Engineering 18 (2022) 161–172

Contents lists available at ScienceDirect

Engineering

journal homepage: www.elsevier.com/locate/eng

Research
Material Science and Engineering—Article

A Novel Hierarchically Lightweight Porous Carbon Derived from Egg White for Strong Microwave Absorption

Zonglin Liu, Xu Zhao, Liangliang Xu, Qingyu Peng *, Xiaodong He *

National Key Laboratory of Science and Technology on Advanced Composites in Special Environments, Center for Composite Materials and Structure, Harbin Institute of Technology, Harbin 150080, China

ARTICLE INFO

Article history:
Received 10 March 2020
Revised 21 May 2021
Accepted 8 June 2021
Available online 27 September 2022

Keywords:
Microwave absorption
Porous carbon
Biomass
K_2CO_3

ABSTRACT

Egg custard is a common dish on the dining table and exhibits a uniform porous structure after freeze-drying. The protein within egg custard is a rich source of carbon and nitrogen, and the custard's unique microstructure and adjustable electrical properties make it a potential porous carbon precursor. Herein, nitrogen *in situ* doped porous carbons (NPCs) and potassium-carbonate-modified NPCs (PNPCs) are obtained through a simple gelation and carbonization process using egg white as the raw material. The unique morphologies of the porous carbon are inherited from the protein and include fibrous clusters, honeycomb holes, and a grooved skeleton. Their excellent impedance matching and effective internal loss make the obtained porous carbons good candidates for lightweight electromagnetic (EM) wave absorbers without the need to dope with metal elements. As a representative porous carbon, PNPC10-700 has multiple structures, including fibrous clusters, honeycomb holes, and a porous skeleton. Moreover, it achieves a maximum reflection loss value of −66.15 dB (with a thickness of 3.77 mm) and a broad effective absorption bandwidth of 5.82 GHz (from 12.18 to 18.00 GHz, with a thickness of 2.5 mm), which surpasses the reported values in most of the literature. Thus, gelation combined with the further carbonization of egg white (protein) is a new method for designing the morphology and EM properties of porous carbon absorbers.

1. Introduction

Porous carbon is lightweight and composition-designable with a highly developed specific surface area and pore structure [1–4]. Due to the excellent electrical conductivity of carbon materials and their unique microstructure, porous carbon has excellent mechanical and electrical properties. Moreover, the microstructure and electrical parameters of porous carbon can be regulated by designing the precursor composition [5] and degree of carbonization [6]. Therefore, porous carbon is widely used in many fields [7], including symmetric supercapacitors [4], thermal management [3,8], electromagnetic (EM) absorption [3], and so forth.

Porous carbon materials are usually prepared through chemical [8,9] or physical [9] self-assembly methods using nanocarbon (i.e., graphene oxide [8], carbon nanotubes [10], etc.), a combination of electrospinning (ES) and chemical vapor deposition (CVD) [11], or the direct carbonization of biomass [4,12,13] or organic aerogel polymers [14,15] in a protective atmosphere. Microwave absorbers have been developed for lighter weight and higher efficiency [16,17]. Thus, porous-carbon-based absorbers [3,5,6,18,19] represent a new generation of EM absorbers, because the preparation of porous carbon permits the dual design of microstructure and components [20]. Unlike conventional EM-absorbing materials, represented by ferromagnetic elements and their oxides [21], porous-carbon-based EM absorbers are lightweight, corrosion-resistant, simple to process, and low in cost [4–6,12,13]. Moreover, porous-carbon-based EM absorbers have designable EM parameters, which ensure a vigorous absorption intensity with a broad effective absorption bandwidth [3,12,13,18,19,22].

Achieving high absorption strength requires good impedance matching, which can be tuned by designing the material's microstructure [16,17] and composition [23,24]. Due to the complexity of the polymerization process, it is challenging to realize a complex microstructure in a simple way in the porous carbon that is obtained via the carbonization of synthetic carbon-containing polymers [14,15]. Moreover, the bottom-up synthesis of porous carbon from nanocarbon (graphene, graphene oxide

* Corresponding authors.
E-mail addresses: pengqingyu@hit.edu.cn (Q. Peng), hexd@hit.edu.cn (X. He).

https://doi.org/10.1016/j.eng.2022.04.026

[8], or carbon nanotubes [10]) involves complex practical steps and usually requires the assistance of templates and activators. In contrast, the carbonization of natural biomass (e.g., pork skin [4], tofu [12], or silk [13]) allows the carbon to artificially retain the original unique microstructure through a simple preparation process. Unlike structures that are assembled by small molecules, as mentioned above, the hierarchical structure inherited from biomass has excellent EM absorption but is difficult to obtain by conventional chemical synthesis. Furthermore, protein-rich biomass has a significant nitrogen and oxygen content—elements whose doping in a carbon lattice has been demonstrated to be advantageous for improving the EM performance [4,25–29]. Aside from urea blending [30] and other impregnation methods, the nitrogen in protein can be *in situ* doped in the carbon skeleton after carbonization, which is more effective and achieves a more uniform result. In other words, by processing protein-containing raw materials through simple pretreatments and subsequent carbonization, the content and distribution of the components and the microstructure of the material can be designed simultaneously.

In contrast to the direct application of biomass for further carbonization, as shown in the literature, we further processed the protein precursors by means of gelation to obtain a porous structure with a more abundant mesoscopic morphology. The mesoscopic form of the prepared porous carbon can be designed artificially rather than allowing it to simply inherit the natural configuration of biomass. In addition, the macroscopic volume of the obtained porous carbon can be artificially regulated from powder to bulk.

To manufacture a more abundant microstructure, the blending of pore-forming agents (i.e., a SiO_2 core [31], potassium hydroxide [4], sodium hydroxide [32], etc.) [4] is usually involved in the preparation of porous carbon. Compared with physical pore formers such as a SiO_2 core [31], chemical agents (e.g., potassium hydroxide [4], sodium hydroxide [32], etc.) eliminate the series of issues caused by physical pore formers, such as particle filling and removal [33]. However, the basicity of potassium hydroxide and sodium hydroxide is too strong. Considering the effect of alkalinity on protein hydrogels [34], potassium carbonate, which has less basicity, was selected as the pore-forming agent in order to achieve a mild pore-forming impact in the subsequent carbonization process. The main reactions involved in the dissolution of potassium carbonate during high-temperature carbonization are as follows:

$$K_2CO_3 \rightarrow CO_2 \uparrow + K_2O \quad (1)$$

$$K_2O + C \rightarrow 2K + CO \uparrow \quad (2)$$

$$2H_2O + 2K \rightarrow 2KOH + H_2 \uparrow \quad (3)$$

$$2KHCO_3 \rightarrow K_2CO_3 + H_2O + CO_2 \uparrow \quad (4)$$

In this work, we adopted a self-assembly method to form porous carbon without metal doping. The porous carbon partly inherits the micromorphology of the protein. Their abundant micromorphology and multiple microstructures grant the nitrogen *in situ* doped porous carbon (NPC) and potassium-carbonate-modified NPC (PNPC) obtained in this work an elegant EM absorption performance, which allows them to serve as lightweight EM absorbers.

2. Materials and methods

2.1. Materials

The egg was bought from a local agricultural market, and we then obtained the egg white by artificially removing the egg yolk. Potassium carbonate was purchased from Tianjin Fengchuan Chemical Reagent Technology Co., Ltd. (China). The reagent was employed without further purification.

2.2. Synthesis of NPCs

The collected egg white was diluted with distilled water to form a protein solution. The amount of water used depended on the mass ratio of egg white to distilled water (e.g., 3:1, 1:1, or 1:0 with no distilled water added). The solution was then dispersed by ultrasound for 3 min and further heated in a water bath at 80 °C for 1 h. In this way, the protein hydrogel was obtained. After freeze-drying and further carbonization at different temperatures (i.e., 600, 700, or 800 °C) with a heating rate of 2 °C·min^{-1} under an argon (Ar) atmosphere, the NPC was obtained.

The as-prepared NPCs are denoted as NPC*a*-*t*, where *a* refers to the mass ratio of egg white to distilled water and *t* refers to the carbonization temperature.

2.3. Synthesis of PNPCs

As the optimal carbonization temperature of the NPCs was found to be 700 °C during the preparation, the carbonization temperature of the PNPCs was set to 700 °C in this work. The rest of the processes were the same as those used for the NPC3-700; however, a specific quantity of K_2CO_3 solution (25 wt%) was added to the protein solution during the initial mixing process, with respective mass ratios of protein to K_2CO_3 of 5:1, 10:1, and 20:1. The as-prepared PNPC samples were denoted as PNPCβ (where β refers to the above ratio), and included PNPC5-700, PNPC10-700, and PNPC20-700.

2.4. Structural and property characterization

The as-prepared NPCs and PNPCs were characterized by means of various techniques. Surface topography images of the porous carbon were obtained via scanning electron microscopy (SEM) using an FEI scanning electron microscope (Helios NanoLab 600i, Thermo Fisher Scientific, USA). A Fourier-transform infrared (FTIR) spectrometer (Nicolet iS50, Thermo Fisher Scientific) was used to analyze the functional groups contained in the samples, such as amine groups, hydroxyl groups, and carboxyl groups. The nitrogen content was characterized by X-ray photoelectron spectroscopy (XPS; ESCALAB 250Xi, Thermo Fisher Scientific). X-ray diffraction (XRD; Empyrean, Malvern Panalytical Ltd., Netherlands) was used to determine the degree of defects in the crystal structure of the samples. The degree of graphitization of the porous carbon was determined using a needle-tip enhanced laser confocal Raman spectroscopy system (inVia Reflex, Renishaw plc, UK). A thermal performance test was performed using a thermogravimetry (TG)/differential scanning calorimetry (DSC) synchronous thermal analyzer (STA 449F, NETZSCH, Germany) to study the thermal stability of the precursor during high-temperature carbonization.

2.5. Characterization of electromagnetic performance

The EM parameters were tested by means of a vector network analyzer (PNA-N5244A, Keysight Tech, USA). Toroidal ring samples were prepared by mixing paraffin with the as-prepared powders (15 wt%); the mixture was then pressed into a mold with an outer diameter (ϕ_{out}) of 7.0 mm and an internal diameter (ϕ_{in}) of 3.0 mm.

3. Results

3.1. Preparation of NPCs and PNPCs

Fig. 1 shows the preparation process of the NPCs and PNPCs and the changes in the microstructure of the porous carbon during carbonization. By controlling the process parameters, a detailed structure with abundant micromorphologies (i.e., fibrous clusters, honeycomb holes, and a grooved carbon skeleton) could be obtained. First, the mixed egg white solution was set in a water bath at 80 °C for gelation. Then, the egg custard was freeze-dried to remove moisture while creating a directional pore structure, which is caused by the squeeze of the ice crystals during the freezing process [35] (Fig. 1(b)). The gelation of the protein and subsequent freeze-drying treatment endowed the precursor with a three-dimensional (3D) macroscopic structure; this directional hollow structure is beneficial for the absorption of EM waves [36]. Afterward, the dried egg custard was set in a tube furnace. The subsequent carbonization enhanced its conductivity for better impedance matching while enriching its microscopic morphology and maintaining the directional microstructure.

During carbonization, the oriented structure in the dry custard (Fig. 1(b)) was partially inherited. More specifically, the small molecules in the egg custard broke down into gases and escaped at high temperatures, leaving tortuous grooves in the skeleton, while the thin-walled parts of the skeleton collapsed into holes (Fig. 1(c) and Fig. S1 in Appendix A). In contrast, the large-molecular-weight protein chains could withstand higher temperatures and were blown into fibers by the airflow created by the decomposition mentioned above (Fig. S2 in Appendix A). Under suitable carbonization conditions, the custard was covered with a thick layer of fibrous clusters (Fig. 1(d) and Figs. S3 and S4 in Appendix A). The obtained porous carbons, which were named NPCs, have multiple structures, including fibrous clusters and a grooved skeleton (Fig. S5 in Appendix A).

When K_2CO_3 was added to the protein solution, the decomposition of the small molecules became more violent, and numerous honeycomb-like voids were left in the porous carbon framework (Fig. 1(e) and Fig. S6 in Appendix A). More protein chains were blown out as the potassium carbonate content increased, and the fibrous clusters became finer. However, when the amount of K_2CO_3 was excessive, this layer no longer existed, as it was destroyed by the large amount of gas released by the violent decomposition. Therefore, by choosing an appropriate amount of potassium carbonate, porous carbons with the multiple morphologies of fibrous clusters, honeycomb holes, and a grooved skeleton could be obtained (Fig. S7 in Appendix A). We called these carbons PNPCs.

3.2. Characterization of the microtopography

The distilled water content, temperature of the carbonization process, and K_2CO_3 doping content are considered to be the three primary parameters of the formation of the porous carbon. To further study the influence of these factors on the porous carbon microstructure, we investigated the morphologies of the NPCs and PNPCs by means of SEM (Fig. 2). It can be concluded that a lower content of distilled water implies a higher content of protein, which results in thicker layers in the porous carbon (Fig. 2(a) and Fig. S4). In addition, the carbonization temperature controls the

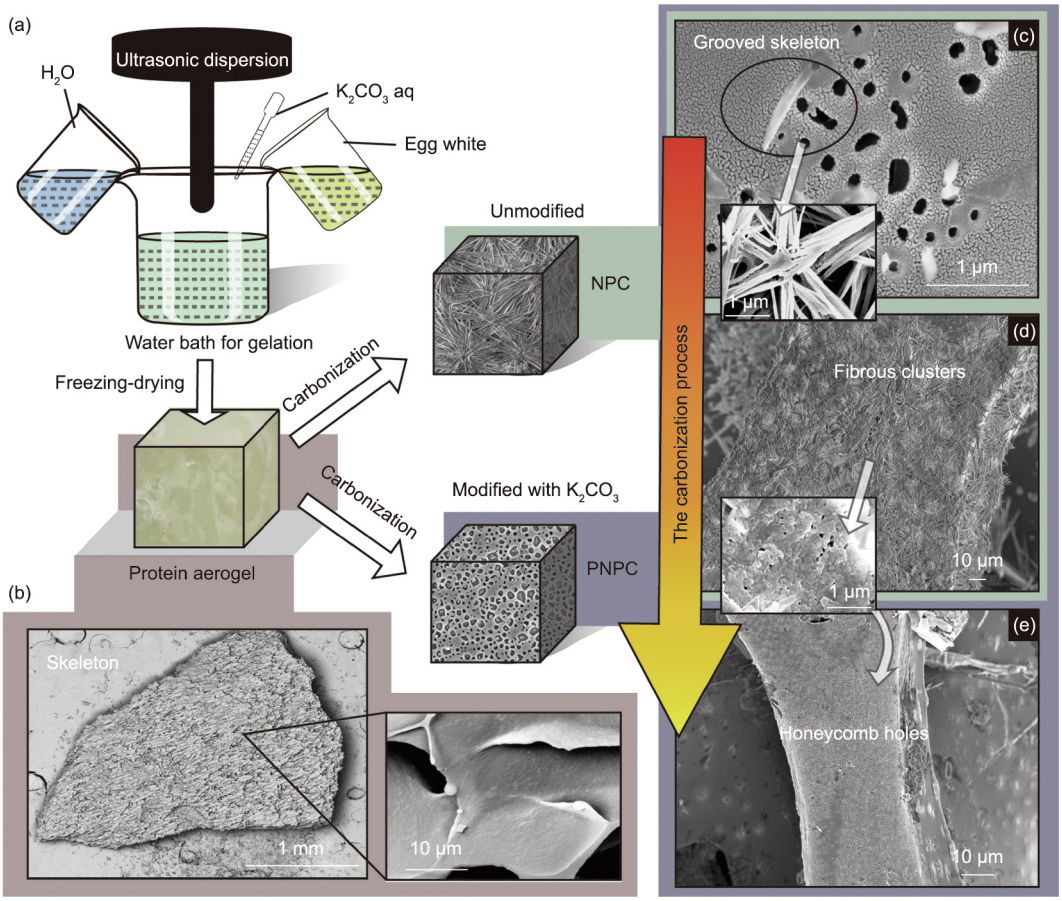

Fig. 1. (a) Schematic of the formation of NPCs and PNPCs (aq: aqueous). (b–e) SEM images of the typical micromorphology of (b) the dry custard, (c, d) the NPC samples, and (c–e) the PNPC samples.

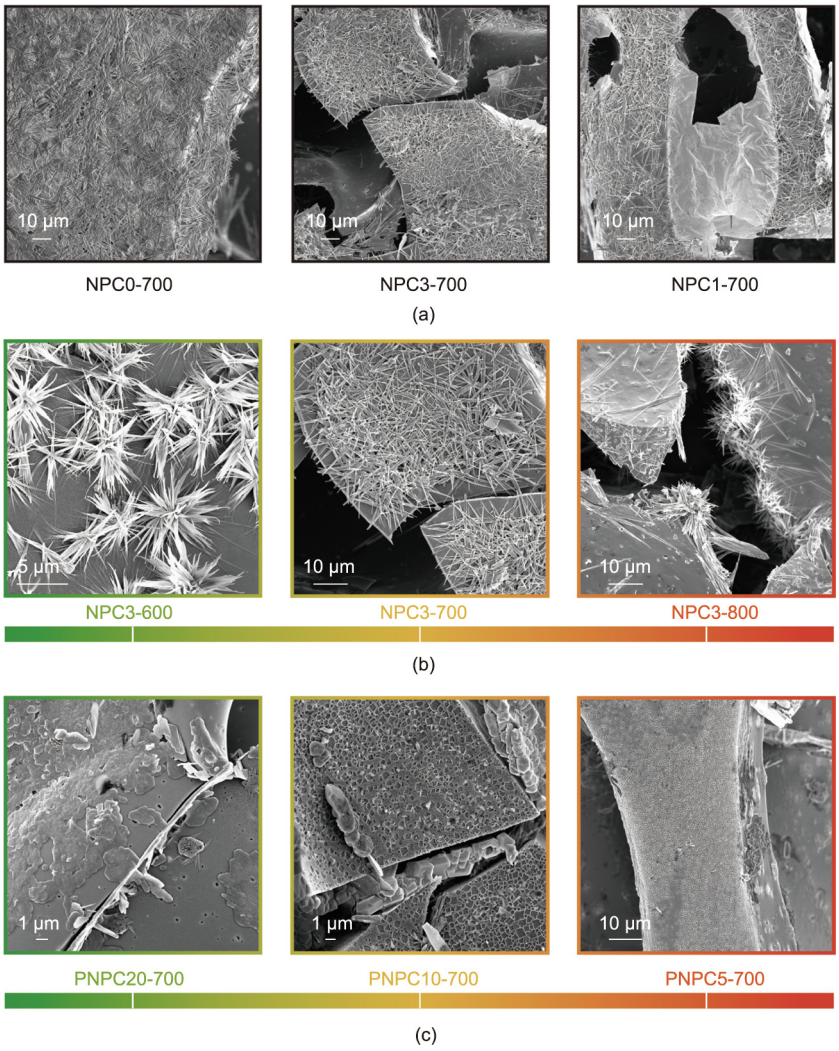

Fig. 2. SEM images of (a) NPCs (NPC0-700, NPC3-700, and NPC1-700) with different distilled water content; (b) NPCs (NPC3-600, NPC3-700, and NPC3-800) obtained through different carbonization temperatures; and (c) PNPCs (PNPC20-700, PNPC10-700, and PNPC5-700) with different K_2CO_3 doping contents obtained at 700 °C.

degree of carbonization, and the K_2CO_3 doping content directs the severity of the carbonization; together, these factors determine the unique morphologies of the porous carbon.

It can be observed in Fig. 2(b) that the NPC samples have the appearance of fibrous clusters and a grooved carbon skeleton, which are inherited from the protein. With an increase in the carbonization temperature, the fibrous-cluster content first increases and then decreases, indicating that there is an optimal carbonization temperature (700 °C; SEM images of NPC0-700 are shown in Fig. S4). At lower temperatures, the escape of small molecules results in a dense layer of fibrous clusters. At higher temperatures, the protein chains are severely carbonized, the structure can no longer be maintained, and the fibrous-cluster morphology disappears.

As for the K_2CO_3 doping content, there is also an optimum K_2CO_3 doping range. With an increase in the doping amount, the proportion of the honeycomb-hole morphology increases, and the fibrous clusters become denser. However, an excessively high doping amount causes the carbonization process to be too violent, which prevents the fibrous clusters from stably existing, leaving a morphology with only honeycomb holes and a grooved skeleton (Fig. 2(c) and Fig. S6). It is foreseeable that regulation of the microstructure of the material would affect the EM performance and could be used to achieve impedance matching, which is consistent with the test results shown in Section 3.3.

3.3. Characterization of electromagnetic performance

As critical physical properties of materials, the permittivity and permeability determine the EM properties and show the impact of altered parameters on material properties. It can be seen in Figs. 3–5 that the permeabilities of the samples obtained by different processes are nearly unchanged, which means that the variation in the performance of the samples mainly depends on the different permittivities.

As shown in Fig. 3, the permittivities of NPC1-600, NPC1-700, and NPC1-800 are positively related to the carbonization temperature. A higher carbonization temperature corresponds to a higher degree of graphitization (i.e., better conductivity), and a higher dielectric loss value can be obtained by raising the carbonization temperature. With an increase in the distilled water content, the porosity of the porous carbon increases and the framework becomes thinner, which results in a decrease in the structural strength of the porous carbon until the protein fails and becomes a gel (Fig. 2(a)). The increase of porosity is beneficial to the carbonization of the precursors [35], leading to higher permittivity

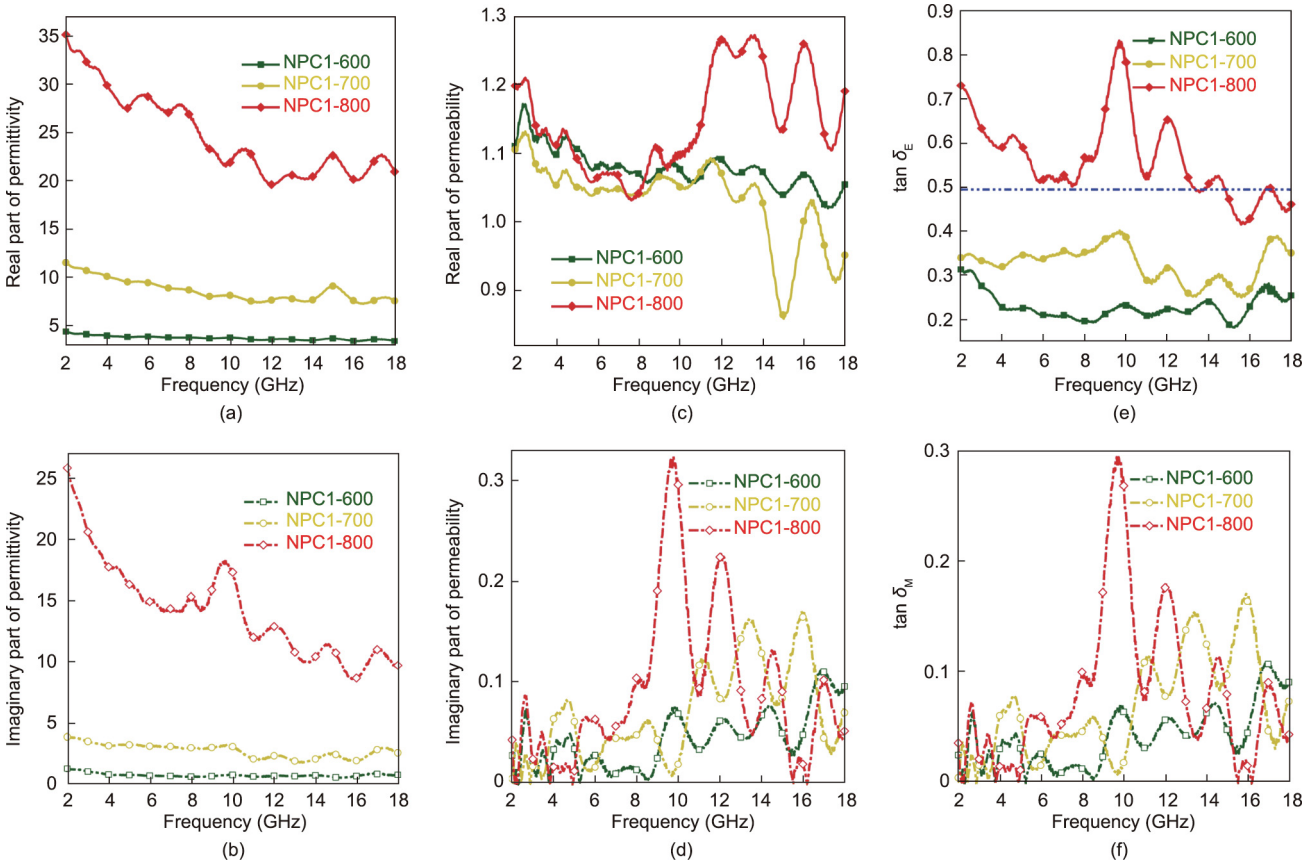

Fig. 3. EM performance of NPCs (NPC1-600, NPC1-700, and NPC1-800) with different carbonized temperatures. (a) Real part and (b) imaginary part of the permittivity of the NPCs; (c) real part and (d) imaginary part of the permeability of the NPCs; (e) tan δ_E (δ_E: dielectric loss) and (f) tan δ_M (δ_M: magnetic loss) of the NPCs.

values. However, a porosity that is too high will affect the continuity of the porous carbon and result in a decrease in the permittivity of the porous carbon (Fig. 4). It can be concluded that there is a preferred value range for the distilled water content, which has a larger tan δ_E value (δ_E is the dielectric loss, the average tan δ_E value of NPC3-700 is over 0.5 in 2–18 GHz) and corresponds to a more effective EM absorption performance.

There is also an optimal range for the potassium carbonate content (PNPC10-700, as shown in Fig. 5). Doping with a suitable amount of potassium carbonate leads to the formation of a microstructure of honeycomb holes with numerous interfaces. However, excess potassium carbonate causes the carbonization process to become too violent, such that the fibrous-cluster morphology can no longer be maintained. As a result, the degree of polarization of the porous carbon is reduced (Fig. 5(a)), and the conductivity of the porous carbon also decreases due to the decrease in the continuity of the porous carbon (Fig. 5(b)).

The experimental results described above demonstrate that the EM parameters of the porous carbon can be designed by adjusting the process parameters to achieve better impedance matching and internal reflection loss (RL), thereby obtaining a better EM absorption performance.

3.4. Chemical characterization

The primary step in the preparation process is the carbonization of the protein precursor, which involves complex chemical reactions. As shown in Fig. 6(a), the TG/DSC result aligns exactly with the results from previous research [37]: As the temperature rises, the mass of the sample decreases, including three stages of the evaporation of water, pyrolysis of proteins, and carbonization of the skeleton. Systematic chemical characterizations, including XRD, Raman spectroscopy, XPS, and FTIR spectroscopy, were also performed to further investigate the degree of carbonization.

To identify the compound structure of the samples, FTIR spectra were obtained. Fig. 6(b) shows the FTIR spectra of NPCs carbonized at different temperatures and of PNPCs with different potassium carbonate doping amounts. Substantial and broad characteristic peaks can be seen at 3240 and 3016 cm^{-1} in the samples, which can be attributed to –OH and –NH, respectively. In addition, the stretching vibration peak of H–C=O at 2918 cm^{-1} and the stretching peaks at 1450–1380 cm^{-1} are caused by the expansion and contraction of C–H. The spectra of the PNPCs confirm that the potassium carbonate modification does not visibly change the type of chemical composition of the porous carbon. Instead, it mainly affects the distribution of the components in the structure of the samples. Moreover, typical reflections from the (002) and (101) planes of the disordered carbon materials at 24° and 40°, respectively, can be observed in the XRD pattern of the samples. As shown in Fig. 6(c), the degree of carbonization corresponds to the regularity of the microstructure, which is consistent with the FTIR results.

To further determine the amount of amorphous carbon in the porous carbon, Raman spectra were obtained. As shown in Fig. 6(d), the D (defect and disorder) and G (graphitic) bands can be observed at around 1320 and 1590 cm^{-1}, respectively. It can be concluded that a relatively lower D/G intensity ratio corresponds to a higher degree of graphitization with fewer defects of the carbon materials [3]. Herein, the D/G intensity ratios of NPC0-600, NPC0-700, NPC0-800, NPC3-700, NPC1-700,

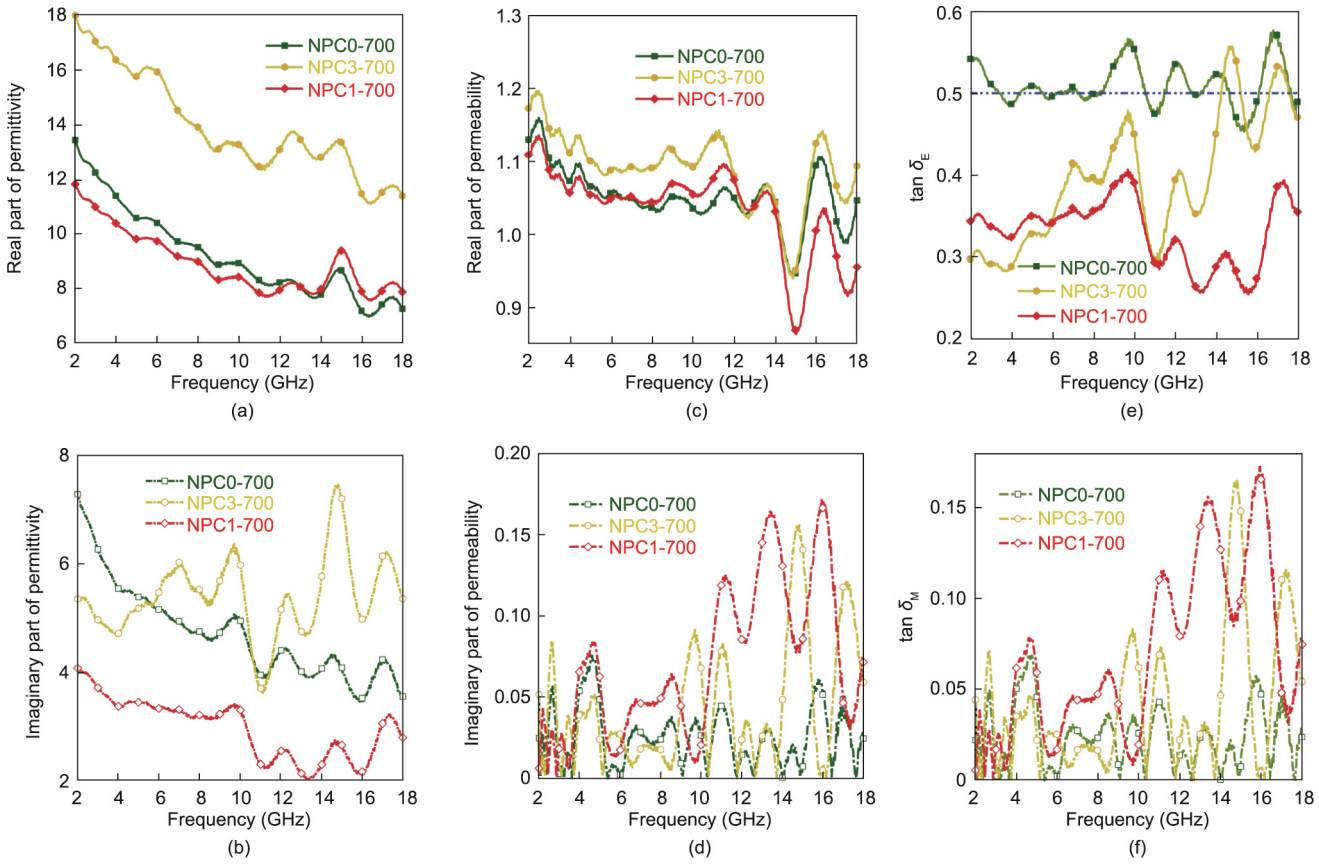

Fig. 4. EM performance of NPCs (NPC0-700, NPC3-700, and NPC1-700) with different distilled water content. (a) Real part and (b) imaginary part of the permittivity of the NPCs; (c) real part and (d) imaginary part of the permeability of the NPCs; (e) tan δ_E and (f) tan δ_M of the NPCs.

PNPC20-700, and PNPC10-700 were determined to be 0.94, 0.97, 0.98, 1.03, 0.95, 1.00, and 0.98, respectively.

Consistent with previous research, a sample that is carbonized at a higher temperature has a higher degree of graphitization [3,38]. As the temperature of carbonization increases, hetero-elements escape in the form of gas, the number of defects in the carbon skeleton decreases, and the degree of graphitization of the system increases. Furthermore, as the degree of graphitization increases, the conductivity of the material increases, which leads to an enhancement of the resistive loss performance [3]. However, when the electrical conductivity rises above the suitable range, the EM absorption drops sharply due to impedance mismatch [6]. As for K_2CO_3 doping for pore formation, the hetero-elements are more likely to escape due to the corrosion of gas, while the microscopic morphology of the obtained porous carbon becomes more detailed. It can be concluded that porous carbon with a certain mass ratio (3:1) of egg white to distilled water results in a relatively higher D/G intensity ratio. Therefore, samples with appropriate degrees of graphitization can be obtained by controlling the process parameters (i.e., the K_2CO_3 doping content, distilled water content, and carbonization temperature).

A surficial element content percentage histogram was carried out using the XPS data. Samples with a relatively higher D/G intensity ratio correlate with a relatively lower percentage of nitrogen and a relatively larger percentage of carbon (Fig. 6(e)). Compared with K_2CO_3 doping and the distilled water content, the carbonization temperature is the main factor affecting the degree of carbonization, which determines the content of each element (including carbon, oxygen, and nitrogen) in the porous carbon. The C 1s, O 1s, and N 1s contents of the samples are as follows: NPC0-600 (44.85%, 50.31%, and 4.84%), NPC0-700 (54.18%, 41.87%, and 3.95%), NPC0-800 (69.97%, 26.26%, and 3.77%), NPC3-700 (56.15%, 39.61%, and 4.24%), NPC1-700 (55.00%, 38.84%, and 6.16%), PNPC20-700 (59.30%, 36.23%, and 4.47%), and PNPC10-700 (61.03%, 35.11%, and 3.86%). The peaks observed in the XPS spectrum prove that the oxygen and nitrogen are successfully doped. In addition, it can be concluded that, when the doping amount of potassium carbonate increases, the nitrogen and oxygen retention rates of the PNPCs decrease. This is because K_2CO_3 doping makes it easier for hetero-elements to escape from the system in the form of gas, so the retention of nitrogen and oxygen is slightly reduced.

As shown in Fig. 6(f), distinct peaks at 531.6, 397.9, and 284.6 eV can be clearly observed in the XPS spectra of the samples; these correspond to the characteristic peaks of O 1s, N 1s, and C 1s, respectively. Significant peaks can also be observed at 497.4 and 292.9 eV, which correspond to the crystals of the sodium and potassium salts. Due to the presence of sodium, the XPS spectrum of the sample has a chemical drift of –1.33 eV [39]. The egg white may also contain a small amount of sulfur, which would be indicated by disulfide bonds in the spectra. However, sulfur cannot be observed in the carbonized samples due to the decomposition that occurs during the high-temperature carbonization.

We take PNPC10-700 as a representative for a detailed discussion, as shown in Figs. 6(g)–(i). The C 1s spectrum (Fig. 6(g)) can be deconvoluted into five individual component peaks: COOH (288.9 eV), C=O (287.8 eV), C–O (286.5 eV), sp^3 C–C (285.6 eV), and sp^2 C=C (284.6 eV) [28,40]. The asymmetry trailing tails in C 1s are caused by the inherent asymmetry of the graphite peaks and the contribution of the oxygen complexes on the surface. The O 1s XPS spectrum (Fig. 6(i)) can also be deconvoluted into four peaks: C–O groups (533.2 eV), COOH groups (532 eV), C=O

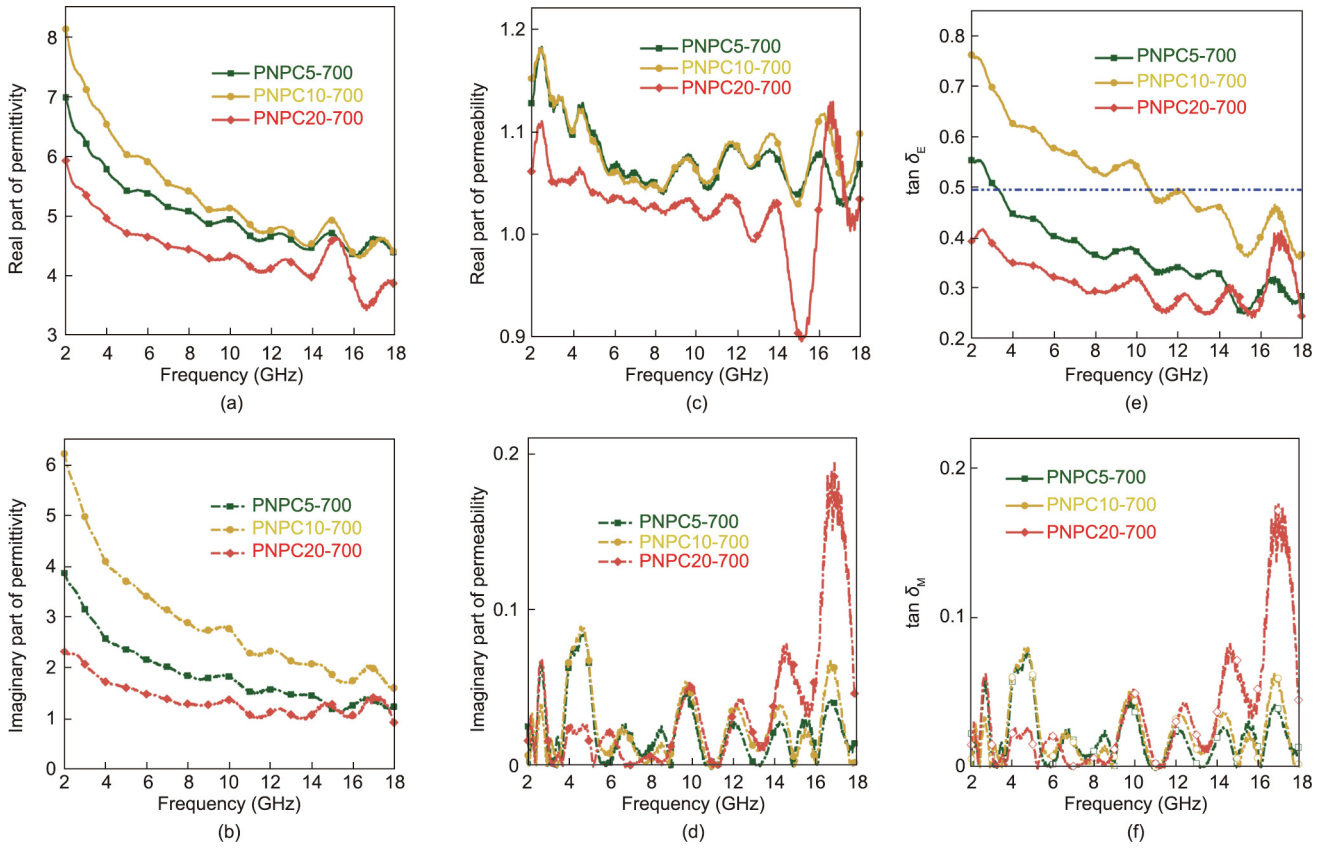

Fig. 5. EM performance of PNPCs (PNPC5-700, PNPC10-700, and PNPC20-700) with different K_2CO_3 doping content. (a) Real part and (b) imaginary part of the permittivity of the PNPCs; (c) real part and (d) imaginary part of the permeability of the PNPCs; (e) tan δ_E and (f) tan δ_M of the PNPCs.

groups (531.7 eV), and hydroxyls (536 eV). Among them, the C=O groups are electrochemically active, which is favorable for improving the EM absorption. Moreover, the N 1s XPS core level spectrum (Fig. 6(h)) demonstrates the existence of three types of nitrogen functionalities: graphitic N (N-4, 400.8 eV), pyrrolic N (N-5, 399.7 eV), and pyridinic N (N-6, 398.0 eV). It has been confirmed that pyrrolic N and pyridinic N can create defects as active sites for EM scattering, while graphitic N can enhance the conductivity of carbon materials [28,29].

Furthermore, nitrogen atom doping can enhance the dipole polarization according to density functional theory (DFT) calculations [26,27]. At the same time, the oxidized groups (carboxyl, hydroxyl, etc.) shown in the XPS data can enha=nce the conductivity of the porous carbon [25]. Thus, by controlling the doping content of oxygen and nitrogen, the EM absorption can be distinctly enhanced.

3.5. EM absorption of NPCs and PNPCs

The samples obtained in this work have excellent EM absorption, with deep RL peaks and wide bandwidths. NPCs and PNPCs with effective absorption in specific frequency bands can be obtained by changing the process parameters.

The RL formula of the EM-absorbing material can be deduced according to transmission line theory and can be expressed as follows [7,41]:

$$Z_{in} = \sqrt{\frac{\mu_r}{\varepsilon_r}} \tanh\left(\frac{j2\pi f d\sqrt{\mu_r \varepsilon_r}}{c}\right) \quad (5)$$

$$RL = 20\log\left|\frac{Z_{in}-1}{Z_{in}+1}\right| \quad (6)$$

where Z_{in} is the EM wave incident impedance of the material, j is the imaginary unit, f is the frequency of the EM wave, d represents the thickness of the material, ε_r and μ_r are the complex permittivity and permeability, respectively, and c is the velocity of light.

The 3D RL curve of the PNPC10-700 sample with different thicknesses in the 2–18 GHz frequency band was calculated according to the RL formula mentioned above (Fig. 7(a), where the red line is the effective absorption threshold curve with a value of RL = −10 dB). The PNPC10-700 sample exhibits excellent broadband EM wave absorption and has a maximum RL value of −66.15 dB at 8.86 GHz with a thickness of only 3.77 mm. With an increase in the sample thickness, the position of the most substantial absorption peak gradually shifts to lower frequencies, while the effective absorption frequency range of RL < −10 dB is extended to the low-frequency range; this aligns with the quarter-wavelength theory, which can be expressed as follows [24]:

$$d = \frac{\lambda_e}{4} = \frac{(n/4)c}{f\sqrt{\mu_r \varepsilon_r}} \ (n = 1, 3, 5, \cdots) \quad (7)$$

where λ_e is the wavelength of the EM wave in the medium and n is an odd number of times of the 1/4 wavelength.

The matching thickness of the sample increases as the frequency of the EM wave decreases, which fits well with the theoretical value, as shown in Fig. 7(b).

The performances of the other samples with different thicknesses are shown in Fig. 7(c), which is a 3D graph ploting the max RL (height), the thickness (width), and the effective absorption bandwidth (depth) of the samples. It can be seen that the NPCs have relatively broader effective absorption bands, while the PNPCs have relatively more massive RL peaks. The effective

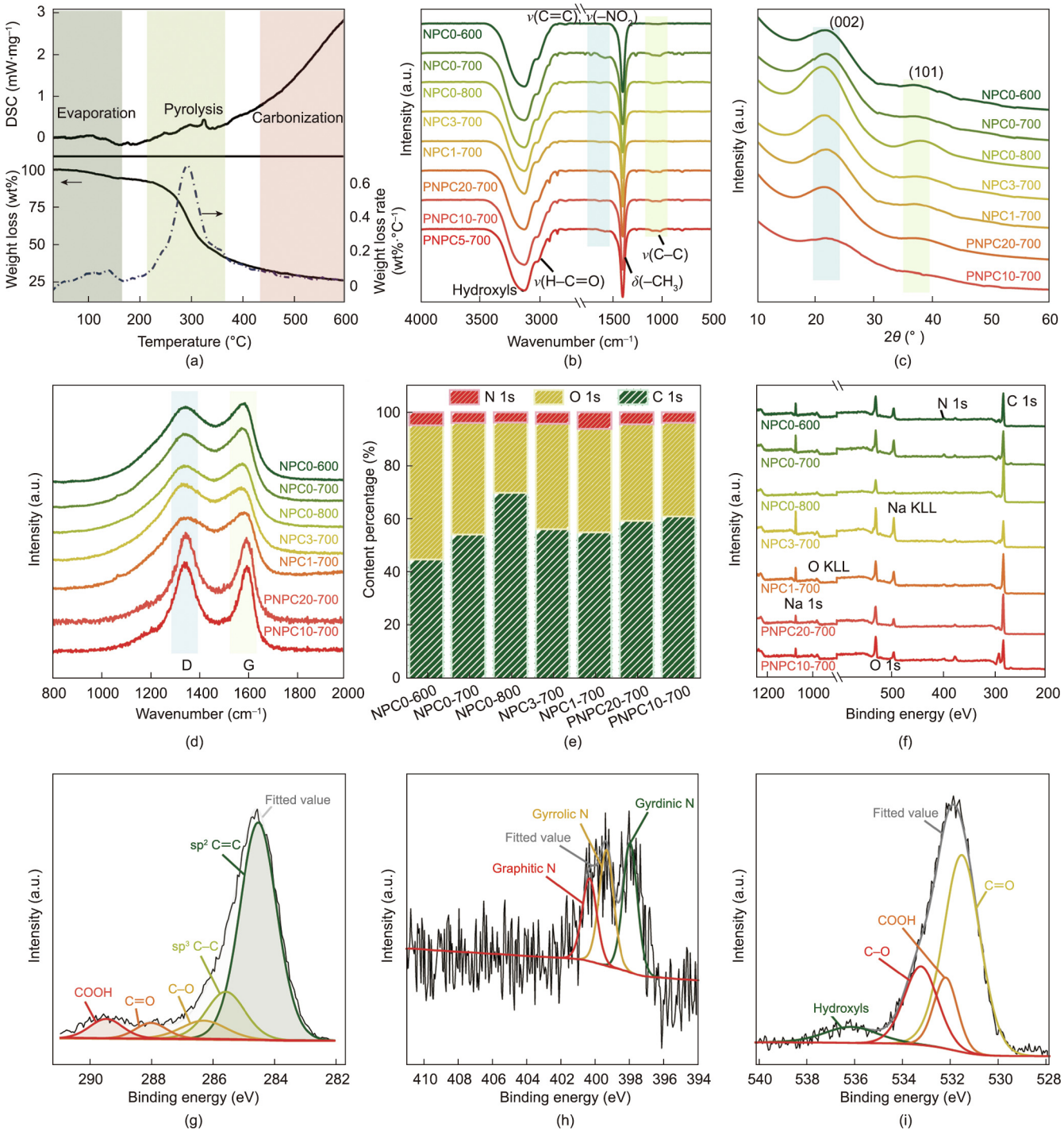

Fig. 6. Chemical characterization of the samples. (a) TG and DSC curves of the freeze-dried protein hydrogel. (b) FTIR spectra, (c) XRD spectra, and (d) Raman patterns (a.u.: arbitrary unit; ν: stretching vibration; δ: bending vibration). (e) Contents of the elements in the samples. (f) XPS total surveys. (g) C 1s, (h) N 1s, and (i) O 1s high-resolution spectra for PNPC10-700.

absorption frequency bands can be adjusted by designing the EM parameters, which is done by controlling the process parameters. In essence, a higher carbonization temperature corresponds to a lower frequency band, a larger amount of distilled water corresponds to a higher frequency band, and the doping of K_2CO_3 lowers the frequency band. Moreover, the effective absorption band narrows as the K_2CO_3 doping content increases.

The Ku band (12–18 GHz) and the X band (8–12 GHz) are widely used in the military field [33]. By controlling the carbonization temperature, distilled water content, and K_2CO_3 doping content, the porous carbon obtained in this work can achieve effective absorption within these specific bands (Fig. 7(d)). Among them, NPC0-700 achieves efficient absorption in 1.9 mm of the whole Ku band, and the RL peak of NPC1-700 reaches more than 30 dB in 1.8 mm for the Ku band. In the X band, PNPC10-700 in 3.4 mm shows a broad absorption band, and the corresponding RL peak reaches more than 60 dB. PNPC20-700 also serves well, while the RL peaks of the NPCs are relatively lower. A comparison of the EM wave absorption of the porous carbon obtained in this work and that of other reported biomass-derived absorbers in

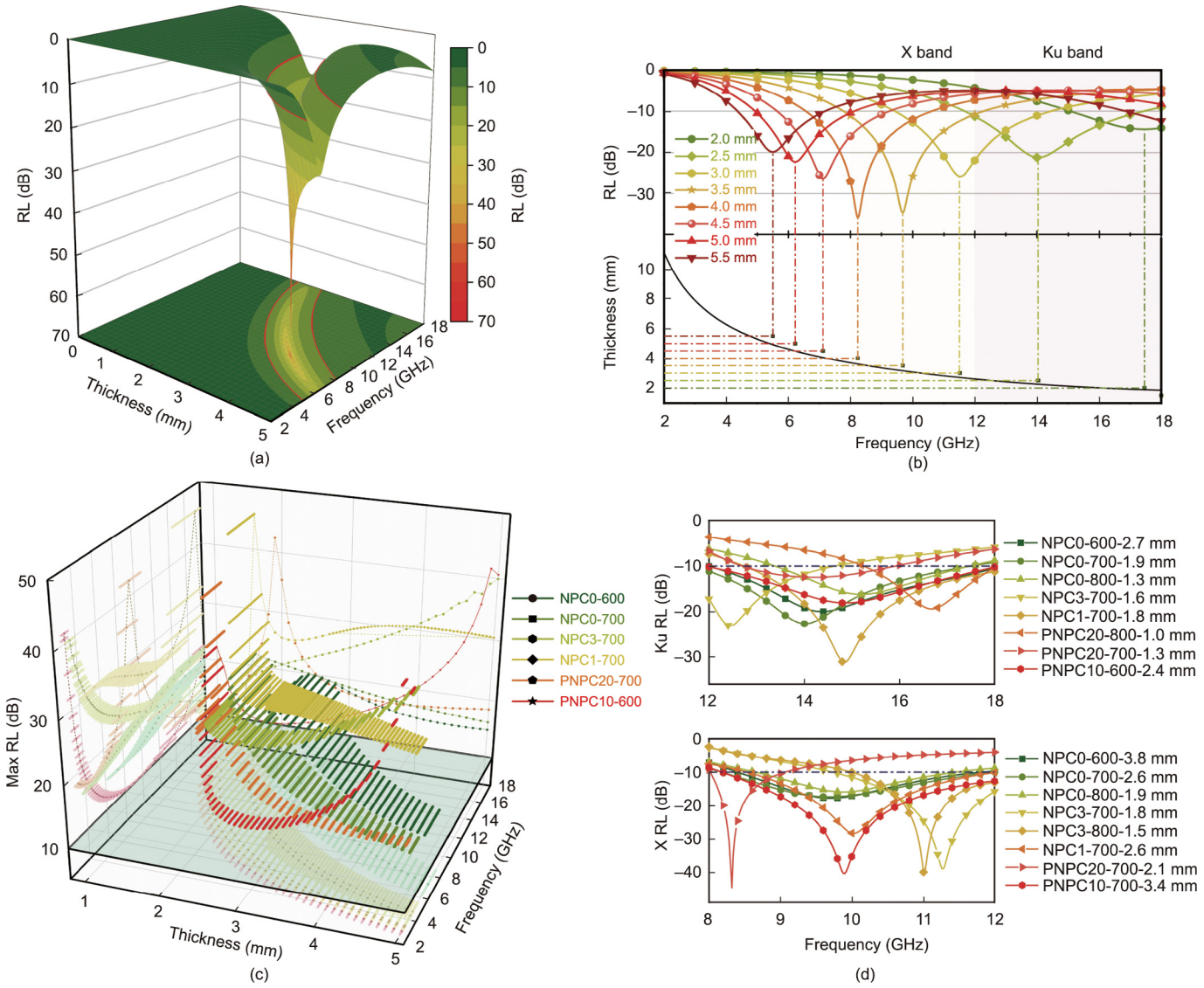

Fig. 7. (a) 3D theoretical RL curve of PNPC10-700; (b) RL peak-thickness curve of PNPC10-700; (c) dependence of thickness and max RL on the EM field of the samples; (d) RL curves in the Ku and X bands.

recent years is provided in Table S1 in Appendix A [1,2,5,6,20,24,32,38,42–45]. The table reveals that the NPCs and PNPCs have excellent absorption strength and a wide effective absorption bandwidth with a low filler loading. Unlike previously reported biomass-derived absorbers, the lightweight NPCs and PNPCs presented here do not rely on ferromagnetic metal doping and have excellent EM absorption properties obtained by manipulating the microstructure.

3.6. EM absorption mechanism of NPCs and PNPCs

Taking PNPC10-700 as an example, we now discuss the material design process in order to reveal the absorption mechanism of the porous carbon obtained in this work. It is well known that the characteristic wave impedance (η) of a material can be expressed as follows:

$$\eta = \sqrt{\frac{\mu_r \mu_0}{\varepsilon_r \varepsilon_0}} \tag{8}$$

where $\mu_0 = 1.257 \times 10^{-6}\ \mathrm{H \cdot m^{-1}}$ and $\varepsilon_0 = 8.854 \times 10^{-12}\ \mathrm{F \cdot m^{-1}}$ are the permittivity and permeability of free space, respectively. In addition, the value of the reflection of EM waves (Γ) vertically incident on the surface of the absorbers from free space can be described as follows:

$$\Gamma = \frac{\eta - \eta_0}{\eta + \eta_0} \tag{9}$$

where $\eta_0 = \sqrt{\mu_0/\varepsilon_0} = 376.73\ \Omega$ is the EM wave impedance in free space. Carbon does not exhibit magnetism, so the ε_r of the porous carbon is usually greater than its μ_r. In order to minimize the reflection of EM waves, apart from introducing magnetic components to increase the μ_r, a small ε_r is desirable in the design of porous carbon absorbers [2]. In this work, the complex hierarchical structure containing numerous micropores and mesopores, which is obtained by adjusting the composition of the precursor and the carbonization temperature, successfully decreases the ε_r. Thus, in this case, $\varepsilon_r \to \mu_r$ (leads to $\Gamma \to 0$), and an excellent impedance matching effect is achieved, which boosts the EM wave absorption of the porous carbon [2].

According to the classical Debye theory, the dielectric behavior can be illustrated by the Cole–Cole model, and the relationship

between the real part (ε') and imaginary part (ε'') of permittivity can be described as follows:

$$(\varepsilon' - \varepsilon_\infty)^2 + (\varepsilon'')^2 = (\varepsilon_s - \varepsilon_\infty)^2 \quad (10)$$

where ε_s and ε_∞ are the stationary dielectric constant and the optical dielectric constant, respectively. The plot of ε'–ε'' is called the Cole–Cole plot, in which a single semicircle represents a Debye relaxation process [46]. According to previous research [47], the larger the radius and number of Cole–Cole semicircles, the stronger the degree of multiple polarization. In Fig. 8(a), at least four semicircles can be observed, showing that the dielectric and resistive losses are the primary parts of the polarization relaxation. The corresponding Cole–Cole semicircle plots of PNPC10-700 at multiple Debye relaxation frequencies are shown in Fig. S8 in Appendix A [48]. Considering the microstructure of PNPC10-700, these relaxation loss mechanisms may include conduction loss in the porous carbon frameworks, dipole polarization induced by nitrogen inherited from the protein, and interface polarization relaxation between the hierarchical microstructures of fibrous clusters, honeycomb holes, a grooved skeleton, and so forth [5,24,49]. In addition, the tail in Fig. 8(a) can be explained as a conduction loss accompanied by the polarization loss process [33]. The existence of multiple dielectric polarization relaxation mechanisms helps to enhance the dielectric loss capability of the material, thereby improving the wave-absorption properties of the porous carbons.

With regard to magnetic loss, the eddy current coefficient (C_0) for PNPC10-700 was calculated using the following equation:

$$C_0 = \mu''(\mu')^2 f^{-1} \quad (11)$$

where μ' is the real part and μ'' is the imaginary part of permeability, respectively.

In the 2–8 GHz frequency band, C_0 decreases with an increase in frequency, accompanied by sharp fluctuation peaks; in the 8–18 GHz frequency band, the C_0 value fluctuates in a small range of 0–0.02 (Fig. 8(b)). The magnetic loss usually includes the eddy current effect, hysteresis, domain wall resonance, and ferromagnetic resonance [2]. In contrast, domain wall resonance and hysteresis losses can be excluded, as they are not in the 2–18 GHz range but occur at lower and higher frequencies, respectively [50]. Therefore, it can be concluded that the natural resonance of PNPC10-700 is the main magnetic loss mechanism in the 2–8 GHz frequency band; in the 8–18 GHz frequency band, the magnetic loss to EM waves occurs due to the eddy current loss [5,24,44].

In addition to the above loss mechanisms, impedance matching (Z_{in}) and attenuation capability (α) are primary conditions to determine the microwave absorption performance [2]. As shown in Eq. (5), when Z_{in} is close to 1, which indicates excellent impedance matching, almost no reflection occurs throughout the attenuation of the incident EM wave. The input impedance of PNPC10-700 with different thicknesses was calculated according to Eq. (5). As shown in Fig. 8(c), it is clear that the Z_{in} values of all the thicknesses increase initially and then decrease with increasing frequency. Moreover, a small-range fluctuation in a wide frequency band at the peak corresponds to an excellent broadband impedance matching, which again confirms that the hierarchical microstructure of PNPC10-700, with fibrous clusters, honeycomb holes, and a grooved skeleton, grants it marvelous impedance matching and thus an excellent EM absorption performance.

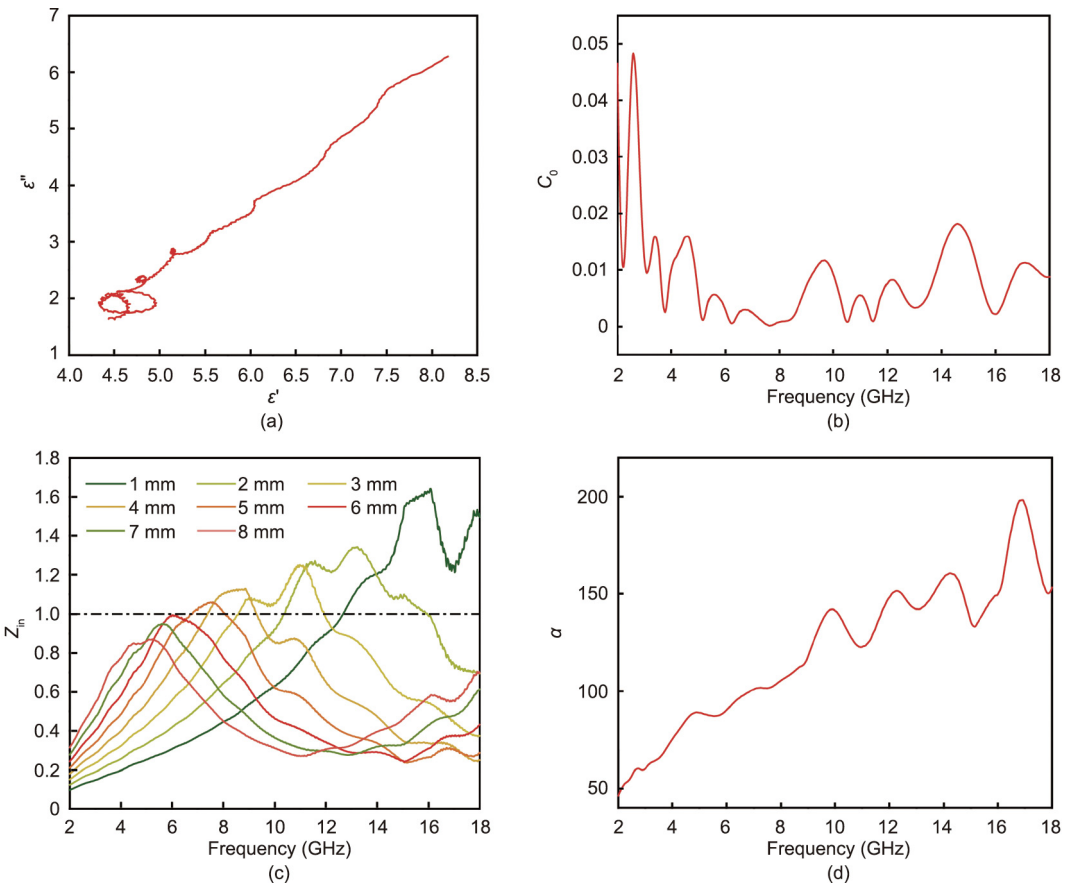

Fig. 8. (a) ε'–ε'' plot, (b) eddy current coefficient (C_0)–frequency (f) curve, (c) normalized characteristic input impedance, and (d) attenuation constant (α) of PNPC10-700.

The attenuation constant (α) is introduced to describe the comprehensive loss competence for materials and can be expressed as follows [51]:

$$\alpha = \frac{2\pi f}{c} \times \sqrt{(\mu''\varepsilon'' - \mu'\varepsilon') + \sqrt{(\mu''\varepsilon'' - \mu'\varepsilon')^2 + (\mu'\varepsilon'' + \mu''\varepsilon')^2}} \quad (12)$$

Larger values of $\tan\delta_E$ ($\tan\delta_E = \varepsilon''/\varepsilon'$) and $\tan\delta_M$ ($\tan\delta_M = \mu''/\mu'$) will result in a more significant attenuation constant (α). It can be observed in Fig. 8(d) that the α value of PNPC10-700 tends to enhance with increasing frequency, and the higher α value is ascribed to the enhanced conductivity.

The previous literature demonstrates that relaxation and conductance contribute to the attenuation of EM waves in composites, and that the two have competing contributions to the attenuation of waves [52,53] and sometimes in the form of synergistic competition [54,55]. Therefore, a beneficial combination of the two can achieve a superior EM absorption performance. The PNPC10-700 obtained in this work possesses an hierarchical microstructure with fibrous clusters, honeycomb holes, and a grooved skeleton, which was achieved by dramatically utilizing the natural structure of proteins. This structure can simultaneously realize impedance matching and a high attenuation constant. Thus, PNPC10-700 exhibits an impressive EM absorption performance in the frequency band of 2–18 GHz.

Furthermore, a probable EM wave-absorption mechanism can be concluded based on the PNPC10-700 sample [7], as shown in Fig. 9. First, the microscopic morphology of the porous carbon is partly inherited from the protein, and gelation gives the porous carbon a 3D framework (Fig. 9(b)). By adjusting the structural design and composition, the multiple structures of the porous carbon can be artificially adjusted to suit different EM wave-absorption scenarios, with superior impedance matching. When a microwave arrives at the porous carbon (Fig. 9(a)), the incident wave easily enters into the surface of the absorber, with only a small amount of the microwave being reflected back. Second, multiple reflection and scattering occurs in the multiple structures of fibrous clusters, honeycomb holes, and a grooved carbon skeleton, extending the propagation paths for the EM microwave and allowing it to be sufficiently attenuated [56]. Third, the fibrous clusters, honeycomb holes, and grooved carbon skeleton provide sufficient heterointerfaces, which are conducive to the formation of interfacial polarization and dipole polarization [26,49]. In addition, the elements in the protein are partially retained, providing active sites for EM scattering within the porous carbon, enhancing the dipole polarization under an alternating EM field, and improving the electrical conductivity of the porous carbon, which endows the porous carbon with an excellent attenuation capability [25–29]. Finally, different parts of the porous carbon have different degrees of graphitization and different electrical conductivities, and these components are dispersed in a complex pore structure equivalent to a resonant circuit (LC circuit). Therefore, an induced current occurs in the circuit due to the time-varying microwave, which can quickly transfer the EM energy into thermal energy, and effective absorption is achieved.

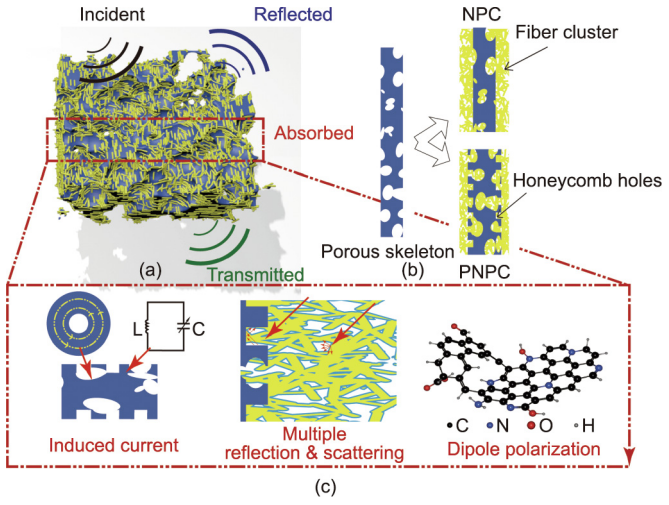

Fig. 9. The probable EM wave-absorption mechanism. (a) Conceptual model of the porous carbon; (b) cross-sectional model of PNPCs; (c) scheme of the microwave attenuation process in the absorber.

4. Conclusions

In summary, we simultaneously optimized the material components and microstructures of porous carbon without the need for ferromagnetic metal elements doping, simply by modulating the K_2CO_3 doping content, distilled water content, and carbonization temperature. Taking full advantage of the natural structure of biomass for the micromorphology design, the porous carbon obtained in this work can achieve effective absorption within specific frequency bands (e.g., the Ku and X bands), with a considerable RL peak value with the proper parameters. In addition, the gelation of the protein provides a simple yet effective process for preparing porous carbon that is environmentally friendly and low in cost.

Acknowledgments

Supported by the Fundamental Research Funds for the Central Universities and Heilongjiang Provincial Natural Science Foundation of China (YQ2020E009).

Compliance with ethics guidelines

Zonglin Liu, Xu Zhao, Liangliang Xu, Qingyu Peng, and Xiaodong He declare that they have no conflict of interest or financial conflicts to disclose.

Appendix A. Supplementary data

Supplementary data to this article can be found online at https://doi.org/10.1016/j.eng.2022.04.026.

References

[1] Zhou X, Jia Z, Feng A, Kou J, Cao H, Liu X, et al. Construction of multiple electromagnetic loss mechanism for enhanced electromagnetic absorption performance of fish scale-derived biomass absorber. Compos Pt B Eng 2020;192:107980.
[2] Wang Y, Di X, Lu Z, Wu X. Rational construction of hierarchical Co@C@NPC nanocomposites derived from bimetallic hybrid ZIFs/biomass for boosting the microwave absorption. J Colloid Interface Sci 2021;589:462–71.
[3] Yuan Y, Ding Y, Wang C, Xu F, Lin Z, Qin Y, et al. Multifunctional stiff carbon foam derived from bread. ACS Appl Mater Interfaces 2016;8(26):16852–61.
[4] Zhou Y, Ren J, Yang Y, Zheng Q, Liao J, Xie F, et al. Biomass-derived nitrogen and oxygen co-doped hierarchical porous carbon for high performance symmetric supercapacitor. J Solid State Chem 2018;268:149–58.
[5] Li F, Xia H, Ni QQ. Egg-white-derived magnetic carbon flakes with enhanced microwave absorption properties. Synth Met 2021;278:116827.
[6] Pan F, Liu Z, Deng B, Dong Y, Zhu X, Huang C, et al. Magnetic Fe_3S_4 LTMCs micro-flowers@ wax gourd aerogel-derived carbon hybrids as efficient and sustainable electromagnetic absorber. Carbon 2021;179:554–65.
[7] Zhao Y, Hao L, Zhang X, Tan S, Li H, Zheng J, et al. A novel strategy in electromagnetic wave absorbing and shielding materials design: multi-responsive field effect. Small Sci 2022;2(2):2100077.
[8] Hu H, Zhao Z, Wan W, Gogotsi Y, Qiu J. Ultralight and highly compressible graphene aerogels. Adv Mater 2013;25(15):2219–23.
[9] Sun H, Xu Z, Gao C. Multifunctional, ultra-flyweight, synergistically assembled carbon aerogels. Adv Mater 2013;25(18):2554–60.

[10] Quan B, Gu W, Sheng J, Lv X, Mao Y, Liu L, et al. From intrinsic dielectric loss to geometry patterns: dual-principles strategy for ultrabroad band microwave absorption. Nano Res 2021;14(5):1495–501.
[11] Liu Y, Luo J, Helleu C, Behr M, Ba H, Romero T, et al. Hierarchical porous carbon fibers/carbon nanofibers monolith from electrospinning/CVD processes as a high effective surface area support platform. J Mater Chem A 2017;5(5):2151–62.
[12] An GH, Kim H, Ahn HJ. Surface functionalization of nitrogen-doped carbon derived from protein as anode material for lithium storage. Appl Surf Sci 2019;463:18–26.
[13] Xiao X, Liu X, Chen F, Fang D, Zhang C, Xia L, et al. Highly anti-UV properties of silk fiber with uniform and conformal nanoscale TiO_2 coatings via atomic layer deposition. ACS Appl Mater Interfaces 2015;7(38):21326–33.
[14] Si Y, Fu Q, Wang X, Zhu J, Yu J, Sun G, et al. Superelastic and superhydrophobic nanofiber-assembled cellular aerogels for effective separation of oil/water emulsions. ACS Nano 2015;9(4):3791–9.
[15] Inagaki M, Qiu J, Guo Q. Carbon foam: preparation and application. Carbon 2015;87:128–52.
[16] Balci O, Polat EO, Kakenov N, Kocabas C. Graphene-enabled electrically switchable radar-absorbing surfaces. Nat Commun 2015;6:6628. Correction in: Nat Commun 2015;6:10000.
[17] Balci O, Kakenov N, Karademir E, Balci S, Cakmakyapan S, Polat EO, et al. Electrically switchable metadevices via graphene. Sci Adv 2018;4(1):eaao1749.
[18] Zhao H, Cheng Y, Liu W, Yang L, Zhang B, Wang LP, et al. Biomass-derived porous carbon-based nanostructures for microwave absorption. Nano-Micro Lett 2019;11(1):24.
[19] Song WL, Cao MS, Fan LZ, Lu MM, Li Y, Wang CY, et al. Highly ordered porous carbon/wax composites for effective electromagnetic attenuation and shielding. Carbon 2014;77:130–42.
[20] Cheng Y, Seow JZY, Zhao H, Xu ZJ, Ji G. A flexible and lightweight biomass-reinforced microwave absorber. Nano-Micro Lett 2020;12(1):125.
[21] Zhang M, Han C, Cao WQ, Cao MS, Yang HJ, Yuan J. A nano-micro engineering nanofiber for electromagnetic absorber, green shielding and sensor. Nano-Micro Lett 2021;13(1):27.
[22] Liang X, Man Z, Quan B, Zheng J, Gu W, Zhang Z, et al. Environment-stable Co_xNi_y encapsulation in stacked porous carbon nanosheets for enhanced microwave absorption. Nano-Micro Lett 2020;12(1):102.
[23] Zhang M, Wang XX, Cao WQ, Yuan J, Cao MS. Electromagnetic functions of patterned 2D materials for micro–nano devices covering GHz, THz, and optical frequency. Adv Opt Mater 2019;7(19):1900689.
[24] Yang M, Yuan Ye, Li Y, Sun X, Wang S, Liang L, et al. Dramatically enhanced electromagnetic wave absorption of hierarchical CNT/Co/C fiber derived from cotton and metal–organic-framework. Carbon 2020;161:517–27.
[25] Cao WQ, Wang XX, Yuan J, Wang WZ, Cao MS. Temperature dependent microwave absorption of ultrathin graphene composites. J Mater Chem C 2015;3(38):10017–22.
[26] Xu H, Yin X, Zhu M, Li M, Zhang H, Wei H, et al. Constructing hollow graphene nano-spheres confined in porous amorphous carbon particles for achieving full X band microwave absorption. Carbon 2019;142:346–53.
[27] Zhao L, He R, Rim KT, Schiros T, Kim KS, Zhou H, et al. Visualizing individual nitrogen dopants in monolayer graphene. Science 2011;333(6045):999–1003.
[28] Liu Y, Shi M, Yan C, Zhuo Q, Wu H, Wang L, et al. Inspired cheese-like biomass-derived carbon with plentiful heteroatoms for high performance energy storage. J Mater Sci Mater Electron 2019;30(7):6583–92.
[29] Elkady OA, Abolkassem SA, Elsayed AH, Hussein WA, Hussein KFA. Microwave absorbing efficiency of Al matrix composite reinforced with nano-Ni/SiC particles. Results Phys 2019;12:687–700.
[30] Quan L, Qin FX, Li YH, Estevez D, Fu GJ, Wang H, et al. Magnetic graphene enabled tunable microwave absorber via thermal control. Nanotechnology 2018;29(24):245706.
[31] Cheng Y, Li Z, Li Y, Dai S, Ji G, Zhao H, et al. Rationally regulating complex dielectric parameters of mesoporous carbon hollow spheres to carry out efficient microwave absorption. Carbon 2018;127:643–52.
[32] Zhou X, Jia Z, Feng A, Wang K, Liu X, Chen L, et al. Dependency of tunable electromagnetic wave absorption performance on morphology-controlled 3D porous carbon fabricated by biomass. Compos Commun 2020;21:100404.
[33] Liu W, Tan S, Yang Z, Ji G. Hollow graphite spheres embedded in porous amorphous carbon matrices as lightweight and low-frequency microwave absorbing material through modulating dielectric loss. Carbon 2018;138:143–53.
[34] Wang L, Liang K, Deng L, Liu YN. Protein hydrogel networks: a unique approach to heteroatom self-doped hierarchically porous carbon structures as an efficient ORR electrocatalyst in both basic and acidic conditions. Appl Catal B 2019;246:89–99.
[35] Job N, Théry A, Pirard R, Marien J, Kocon L, Rouzaud JN, et al. Carbon aerogels, cryogels and xerogels: influence of the drying method on the textural properties of porous carbon materials. Carbon 2005;43(12):2481–94.
[36] Yuan Y, Liu L, Yang M, Zhang T, Xu F, Lin Z, et al. Lightweight, thermally insulating and stiff carbon honeycomb-induced graphene composite foams with a horizontal laminated structure for electromagnetic interference shielding. Carbon 2017;123:223–32.
[37] Orsini S, Duce C, Bonaduce I. Analytical pyrolysis of ovalbumin. J Anal Appl Pyrolysis 2018;130:62–71.
[38] Zhao H, Cheng Y, Lv H, Ji G, Du Y. A novel hierarchically porous magnetic carbon derived from biomass for strong lightweight microwave absorption. Carbon 2019;142:245–53.
[39] Faraci G, La Rosa S, Pennisi AR, Margaritondo G. Na hyperoxidation states studied by core-level spectroscopy. Phys Rev B 1994;50(3):1965–8.
[40] Yang Z, Li Z, Ning T, Zhang M, Yan Y, Zhang D, et al. Microwave dielectric properties of B and N co-doped SiC nanopowders prepared by combustion synthesis. J Alloys Compd 2019;777:1039–43.
[41] Liu X, Chen Y, Cui X, Zeng M, Yu R, Wang GS. Flexible nanocomposites with enhanced microwave absorption properties based on Fe_3O_4/SiO_2 nanorods and polyvinylidene fluoride. J Mater Chem A 2015;3(23):12197–204.
[42] Hou T, Jia Z, Feng A, Zhou Z, Liu X, Lv H, et al. Hierarchical composite of biomass derived magnetic carbon framework and phytic acid doped polyanilne with prominent electromagnetic wave absorption capacity. J Mater Sci Technol 2021;68:61–9.
[43] Huang L, Li J, Wang Z, Li Y, He X, Yuan Y. Microwave absorption enhancement of porous $C@CoFe_2O_4$ nanocomposites derived from eggshell membrane. Carbon 2019;143:507–16.
[44] Guo Z, Ren P, Zhang F, Duan H, Chen Z, Jin Y, et al. Magnetic coupling N self-doped porous carbon derived from biomass with broad absorption bandwidth and high-efficiency microwave absorption. J Colloid Interface Sci 2022;610:1077–87.
[45] Gu Y, Dai P, Zhang W, Su Z. Fe_3O_4 nanoparticles anchored on hierarchical porous carbon derived from egg white for efficient microwave absorption performance. Mater Lett 2021;304:130624.
[46] Lv H, Guo Y, Wu G, Ji G, Zhao Y, Xu ZJ. Interface polarization strategy to solve electromagnetic wave interference issue. ACS Appl Mater Interfaces 2017;9(6):5660–8.
[47] Lv H, Yang Z, Ong SJH, Wei C, Liao H, Xi S, et al. A flexible microwave shield with tunable frequency-transmission and electromagnetic compatibility. Adv Funct Mater 2019;29(14):1900163.
[48] Wang X, Shu JC, He XM, Zhang M, Wang XX, Gao C, et al. Green approach to conductive PEDOT:PSS decorating magnetic-graphene to recover conductivity for highly efficient absorption. ACS Sustain Chem Eng 2018;6(11):14017–25.
[49] Gao Z, Xu B, Ma M, Feng A, Zhang Y, Liu X, et al. Electrostatic self-assembly synthesis of $ZnFe_2O_4$ quantum dots ($ZnFe_2O_4$@C) and electromagnetic microwave absorption. Compos Pt B Eng 2019;179:107417.
[50] Wang Y, Di X, Wu X, Li X. MOF-derived nanoporous carbon/Co/Co_3O_4/CNTs/RGO composite with hierarchical structure as a high-efficiency electromagnetic wave absorber. J Alloys Compd 2020;846:156215.
[51] Lu B, Huang H, Dong XL, Zhang XF, Lei JP, Sun JP, et al. Influence of alloy components on electromagnetic characteristics of core/shell-type Fe–Ni nanoparticles. J Appl Phys 2008;104(11):114313.
[52] Wen B, Cao M, Lu M, Cao W, Shi H, Liu J, et al. Reduced graphene oxides: light-weight and high-efficiency electromagnetic interference shielding at elevated temperatures. Adv Mater 2014;26(21):3484–9.
[53] Cao MS, Wang XX, Zhang M, Shu JC, Cao WQ, Yang HJ, et al. Electromagnetic response and energy conversion for functions and devices in low-dimensional materials. Adv Funct Mater 2019;29(25):1807398.
[54] Wang XX, Cao WQ, Cao MS, Yuan J. Assembling nano–microarchitecture for electromagnetic absorbers and smart devices. Adv Mater 2020;32(36):2002112.
[55] Cao M, Wang X, Cao W, Fang X, Wen B, Yuan J. Thermally driven transport and relaxation switching self-powered electromagnetic energy conversion. Small 2018;14(29):1800987.
[56] Yin Y, Liu X, Wei X, Yu R, Shui J. Porous CNTs/Co composite derived from zeolitic imidazolate framework: a lightweight, ultrathin, and highly efficient electromagnetic wave absorber. ACS Appl Mater Interfaces 2016;8(50):34686–98.